Received: 21 February 2022 | Revised: 10 April 2022 | Accepted: 15 April 2022

DOI: 10.1002/esp.5387

RESEARCH ARTICLE

ESPL WILEY

# Using calibrated surface roughness dating to estimate coastal dune ages at K'gari (Fraser Island) and the Cooloola Sand Mass, Australia

Nicholas R. Patton[1,2] | James Shulmeister[1,2] | Tammy M. Rittenour[3] | Peter Almond[4] | Daniel Ellerton[2,5] | Talitha Santini[6]

[1]School of Earth and Environment, University of Canterbury, Christchurch, New Zealand

[2]School of Earth and Environmental Sciences, The University of Queensland, Brisbane, Australia

[3]Department of Geology, Utah State Luminescence Laboratory, Utah State University, Logan, UT, USA

[4]Department of Soil and Physical Sciences, Lincoln University, Christchurch, New Zealand

[5]Department of Geological Sciences, Stockholm University, Stockholm, Sweden

[6]School of Agriculture and Environment, The University of Western Australia, Perth, Australia

**Correspondence**
Nicholas R. Patton, School of Earth and Environment, University of Canterbury, Christchurch 8140, New Zealand.
Email: nicholas.patton@pg.canterbury.ac.nz

## Abstract

Here we present a novel application of landscape smoothing with time to generate a detailed chronology of a large and complex dune field. K'gari (Fraser Island) and the Cooloola Sand Mass (CSM) dune fields host thousands of emplaced (relict) and active onlapping parabolic dunes that span 800 000 years in age. While the dune fields have a dating framework, their sheer size (~1930 km$^2$) makes high-resolution dating of the entire system infeasible. Leveraging newly acquired ($n = 8$) and previously published ($n = 20$) optically stimulated luminescence (OSL) ages from K'gari and the CSM, we estimate the age of Holocene dunes by building a surface roughness ($\sigma_C$)–age relationship model. In this study, we define $\sigma_C$ as the standard deviation of topographic curvature for a dune area and we demonstrate an exponential relationship ($r^2 = 0.942$, RMSE = 0.892 ka) between $\sigma_C$ and timing of dune emplacement on the CSM. This relationship is validated using ages from K'gari. We calculate $\sigma_C$ utilizing a 5 m digital elevation model and apply our model to predict the ages of 726 individually delineated Holocene dunes. The timing of dune emplacement events is assessed by plotting cumulative probability density functions derived from both measured and predicted dune ages. We demonstrate that both dune fields had four major phases of dune emplacement, peaking at <0.5, ~1.5, ~4, and ~8.5 ka. We observe that our predicted dune ages did not create or remove major events when compared to the OSL-dated sequence, but instead reinforced these patterns. Our study highlights that $\sigma_C$–age modelling can be an easily applied relative or absolute dating tool for dune fields globally. This systematic approach can fill in chronological gaps using only high-resolution elevation data (3–20 m resolution) and a limited set of dune ages.

**KEYWORDS**
dune chronology, dune emplacement, dune stabilization, Holocene, OSL dating, parabolic dune, quaternary, sea-level change

## 1 | INTRODUCTION

Coastal dunes are important environmental systems that are found globally around both seas and lakes (Lancaster et al., 2016; Martínez & Psuty, 2004; Yan & Baas, 2015) and provide a rich record of climatic, geologic, and geomorphic information (e.g. Lindhorst & Betzler, 2016; Patton et al., 2022; Pye, 1983; Swezey, 2001; Wells & Goff, 2007). However, uncovering and deciphering the information from these systems is challenging because they lie at the interface of terrestrial, aquatic, and atmospheric processes, which vary on decadal to millennial timescales (Pye, 1983).

The timing and mechanisms of dune-field activation and consequent stabilization (dune emplacement hereafter) are ascribed to changes in climate and sediment supply, which affect vegetation, storminess, fire frequency, sea-surface temperatures, and sea level (e.g. Han et al., 2021; Shumack & Hesse, 2018; Vimpere et al., 2021; Yan & Baas, 2017). These interpretations have largely been demonstrated on active and/or recently emplaced sections of dune fields, where physical measurements or repeat aerial/satellite imagery are available (e.g. Levin et al., 2017; Marín et al., 2005; Tsoar, 2005). These mechanisms have been extended to emplaced dune systems; however, the direct landscape–process relationship is unknown and it is difficult to infer these processes unless a strong chronological framework is established.

Coastal dune fields' temporal relationships appear chaotic, and it is difficult to determine whether emplaced dunes were once active simultaneously or asynchronously across the dune field. Stochastic (random) dune activity can be indicative of local perturbations but not related to regional changes in environmental conditions, because dunes can simultaneously be active and emplace under the same conditions (Yizhaq et al., 2007). In contrast, mass activation or emplacement of entire dune fields may provide clues about regional environmental forcings (e.g. Lees, 2006). While the direct dating of dunes can be achieved using optically stimulated luminescence (OSL) and/or radiocarbon dating, these techniques are costly and finding suitable dating targets for radiocarbon is often challenging. To offset these limitations, it is common to either establish geobotanical chronosequences (morphological, biological, or pedological units) (e.g. Shulmeister & Lees, 1992; Thompson, 1981), or date organic-rich sediments in adjacent deposits as a means to help place the dunes into a chronosequence (e.g. Wilson, 2002). In both scenarios, these estimates often have large spatial and temporal uncertainty, even in locations where there are clear sequences of onlapping dunes (e.g. Lees, 2006; Swezey, 2001). Consequently, dune sequences that are composed of tens or even thousands of individual dunes are typically secured by only a handful of ages, with wide age constraints that can lead to misinterpretation (e.g. Ward, 2006).

In order to validate age inferences, and hence improve our understanding of former dune activation and stabilization, a means of extending dune ages to all (or most) dunes within a dune field would be a useful tool. In this paper, we explore the implications of recently observed relationships between dune surface roughness ($\sigma_C$) and dune age to explain landscape smoothing with time. We test whether this provides a basis for dating dunes where high-resolution elevation data and a rough geochronological framework are in place.

## 2 | BACKGROUND

### 2.1 | Surface roughness as a proxy for landform age

In most aeolian research, surface roughness characterizes the near-surface meteorological boundary layer over dunes as a means to understand airflow and sediment transport (e.g. Gillette & Stockton, 1989; Jerolmack et al., 2012; Lancaster & Baas, 1998; Levin et al., 2008; Pelletier, 2013; Raupach et al., 1993; Wiggs et al., 1996). For this study, surface roughness is used to measure and define a dune's topographic development (colluvial not aeolian processes). Surface roughness has been defined as a metric of topographic variability (local relief) within a defined spatial area or window (e.g. Korzeniowska et al., 2018). Its application has been utilized across earth science disciplines as a metric to identify and map spatial patterns and as a surrogate to build empirical relationships (Smith, 2014). An important application of $\sigma_C$ is its utility as a proxy for relative age. This relationship has been predominantly applied to constrain the timing of landslide deposition (e.g. Bell et al., 2012; Booth et al., 2009, 2017; Glenn et al., 2006; Goetz et al., 2014; LaHusen et al., 2020; McKean & Roering, 2004), but has also been used on alluvial fans (Frankel & Dolan, 2007), earth flows (Schanz & Colee, in review), and planetary surfaces (Pommerol et al., 2012).

Surface roughness gradually smooths due to diffusive processes of sediment transport (Booth et al., 2017; Patton et al., 2022). The basic principle is that local relief reduces with time due to weathering and erosion, such that features smooth (ridges erode and valleys fill) on surfaces that are not affected by advective processes (e.g. sediment transport by water-driven processes). LaHusen et al. (2020) utilized this principle to build a $\sigma_C$–age relationship from a minimal set of dated landslide deposits and predicted ~10 000 ages in the Pacific Northwest, USA. The utility of this model was not only that ages could be predicted, but more particularly that previously undated landforms could be placed into the context of regional records of climate and landscape change. Consequently, they determined that rainfall, not earthquake activity, was the major driver of landslide activation inland of the Cascadia Subduction Zone.

### 2.2 | Surface roughness in dune systems

Surface roughness has been used to map dune landforms (e.g. Korzeniowska et al., 2018); however, the application of $\sigma_C$ as an indicator of landform age ($\sigma_C$–age relationship) has not yet been applied and tested in a dune system. A recent study by Patton et al. (2022) highlighted the utility of $\sigma_C$ within the Cooloola Sand Mass (CSM) dune field as an important metric, and to characterize and define the stage of geomorphologic development of dune forms. They demonstrated that dune $\sigma_C$, as measured by standard deviation of curvature for a given dune area, could be related to sediment transport theory. They found that dunes are initially emplaced with remarkably uniform surface roughness, which smooths with time, and this evolution can be simulated using a combination of non-linear and linear sediment transport models (Figure 1).

In their study, they determined that dunes evolve in two distinct phases (Figure 1c). The first phase occurs within ~1 kyr after dune emplacement and is explained through non-linear sediment transport. This is a period when dune gradients and $\sigma_C$ are large, erosion and deposition rates are more rapid, and there is a wider variety of transport styles. During this initial period, dune-surface gradients are lowered as a result of disturbance-driven perturbations such as fires and storms. These disturbances may remove vegetation, increase hydrophobicity, and consequently increase the soil's efficiency to move downslope, promoting dry ravel and sheetwash processes (similar to avalanching and grain flows observed on active dune slip faces). This phase continues until dune relief is lowered and $\sigma_C$ values reach the 'transitional zone', as seen in Figure 1c. This zone was defined by

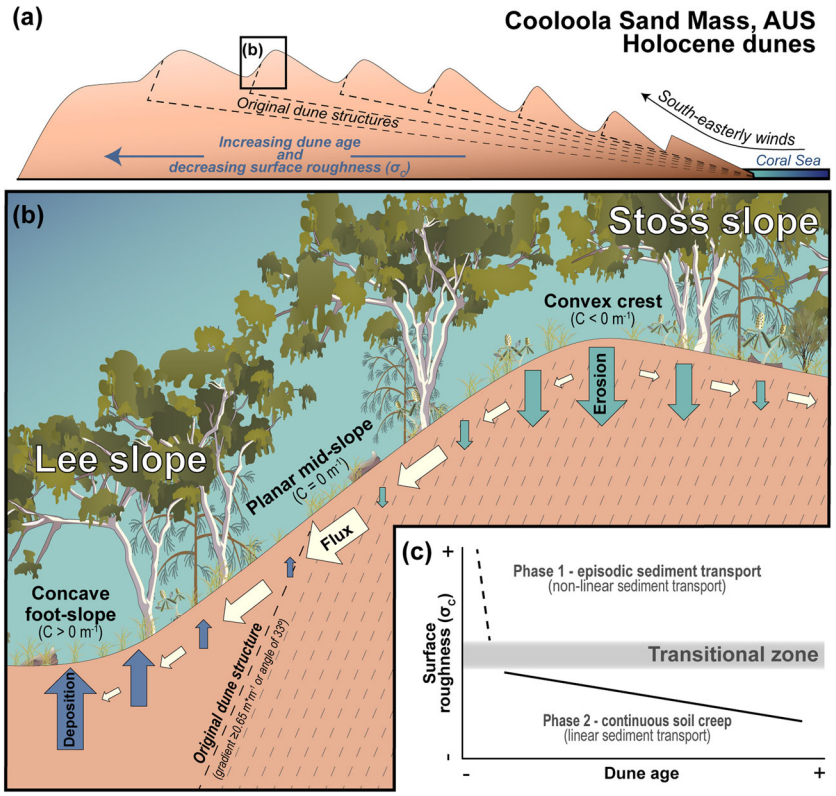


**FIGURE 1** Conceptual diagram and result summary from Patton et al. (2022) between surface roughness ($\sigma_C$) and dune age within the Cooloola Sand Mass (CSM) dune field, Australia. (a) An idealized elevation profile of the CSM dune field. The dunes move inland from the coast through sclerophyll forest and over antecedent topography (dashed lines) via the dominant south-easterly wind. Dunes are emplaced when wind speeds decrease and vegetation stabilizes the dune surface. With every successive dune emplacement, antecedent topography gradients generally increase, thereby decreasing the distance dunes travel inland whilst preserving older dunes. Consequently, most dunes increase in age while decreasing in $\sigma_C$ moving away from the coast. (b) Conceptual diagram of hillslope positions as defined by curvature (*C*) and the contribution of erosion, deposition, and flux (size of arrow). All sediment removed from crest can be accounted for in the foot-slopes (a closed system). As time progresses, ridges lower and hollows fill, reducing hillslope gradients and the maximum and minimum curvature values, thus decreasing dune $\sigma_C$. (c) The general relationship between dune age, surface roughness, and sediment transport phases. Dunes with high $\sigma_C$ (phase 1) are best explained through non-linear sediment transport where episodic processes such as dry ravelling and sheet washing (comparable to grain flows and/or avalanching) occur. Once dune gradients are lowered below their angle of repose (gradient of 0.65 m m$^{-1}$ or angle of 33°) associated with the defined 'transitional zone', sediment transport is limited to slow and continuous processes (phase 2) where their evolution can be explained with linear sediment transport

an observed shift in dominant transport style and the absence of gradients greater than the sand's angle of repose (33°, or gradients of 0.65 m m$^{-1}$). Once gradients are lowered beyond this zone, the second phase of dune evolution begins; wherein sediment transport is proportional to hillslope gradient (linear sediment transport). During this period, dune $\sigma_C$ is small and sediment transport is limited to slow and continuous processes (e.g. biogenic soil creep, rain-splash, and granular relaxation), where erosion occurs at the dune crests and sediment is deposited within the adjacent foot-slopes (Figure 1b). This mechanism is inferred to continue until all relief is either removed or increased due to dune activation or sea-level fall.

Patton et al. (2022) alluded to an apparent exponential relationship between dune $\sigma_C$ and age; however, they chose not to prescribe a single function to explain the dune field's evolution. Instead, they elected to retain the two distinct erosional phases to ensure sediment transport processes were not conflated. Despite this decision, they argued that because the dune fields have limited hillslopes that exceed the angle of repose and a dominance of linear sediment transport, dune $\sigma_C$ will smooth with time and ascribing a single exponential fit is appropriate.

The goal of this study is to test and, if appropriate, apply $\sigma_C$–age modelling to a pair of adjacent coastal dune fields, the CSM and K'gari (Fraser Island) in southeast Queensland. These large and once connected systems are dominated by active and emplaced parabolic dunes. At the CSM, many of these dunes have been dated and the younger parabolic sequences span the Mid- to Late Holocene. Once emplaced, the evolution of the dunes (erosion and deposition) is controlled by a limited set of known diffusional processes that are morphologically trackable through time. We first establish a $\sigma_C$–age relationship on the CSM and test its validity on K'gari. If the model proves to be successful for the dated dunes, we will utilize it to estimate the ages of the remaining Holocene-age dunes in both dune fields. Although our study focuses specifically on two locations, the research provides insights on the evolution of onlapping coastal dune systems and a means to produce a more complete chronological framework for multi-phase dune fields globally.


**FIGURE 2** (a) Satellite imagery of K'gari (Fraser Island) and the Cooloola Sand Mass (CSM), which make up the northern section of the southeast Queensland (SEQ) dune field in Australia. The dune sediments are derived from the longshore drift system (dashed line and arrow) that is delivered to the coast by the dominant south-easterly winds (small arrows). (b) Close-up imagery of the coastline and dunes on K'gari. Photo credit: Jürgen Wallstabe

### 2.3 | Site description: K'gari and Cooloola Sand Mass

The southeast Queensland (SEQ) dune fields in Australia (Figure 2) are composed of K'gari (Fraser Island) and the mainland-attached CSM immediately to the south. The dune fields have been developing for over 800 kyr (Ellerton et al., 2020; Walker et al., 2018). These dune systems are currently separated by the entrance to the Great Sandy Strait and the Inskip Peninsula, but recent work (Köhler et al., 2021) has demonstrated that this separation dates back only to the early Mid-Holocene. Stretching for more than 200 km of coastline (26.17–24.41°S), these two systems cover a combined land area of ~1930 $km^2$, with most of the dune fields on K'gari. They contain one of the longest and most complete coastal dune field sequences in the world (Thompson, 1981) and include over 700 Holocene dunes (Patton et al., 2019; Ward, 2006) covering roughly 640 $km^2$, which are the focus of this study.

Both dune fields have nearly limitless sediment supply, with an estimated 500 000 $m^3$ of sediment transported yearly along the regional longshore drift system (Boyd et al., 2008; Patterson & Patterson, 1983). The parent material is a uniform 98% medium to fine quartz sand (180–250 μm) that is well sorted and sub-rounded to rounded (Thompson, 1992). The majority of onlapping dunes are parabolic with local transgressive dune waves, which travel inland under the influence of the dominant south-easterly winds (Coaldrake, 1962; Ellerton et al., 2018). The region has been tectonically inactive (Roy & Thom, 1981), with only minor variability in local base level, between +2 and −0.5 m since the Holocene sea-level highstand (Lewis et al., 2008). The vegetation communities have been relatively stable (e.g. Atahan et al., 2015; Moss et al., 2013) with tall open/close sclerophyll forest making up the majority of the inland vegetation and coastal scrubland dominating the eastern side of the dune fields (Harrold et al., 1987). Additionally, the climate has remained subtropical (Cfa) during this period (Donders et al., 2006).

## 3 | METHODS

### 3.1 | Dune mapping and remote sensing

In this study, we individually remap the Holocene and modern dunes for both the K'gari and the CSM. Dunes were identified using a 1 m-resolution digital elevation model (DEM) derived from LiDAR (publicly available from Geoscience Australia; Fraser Coastal Project), 1:5000 orthophoto imagery retrieved from Queensland Globe, and field observations. Each dune was delineated by hand in ArcGIS (version 10.6) at the base of slip faces and trailing arms, and defined as polygons.

### 3.2 | Calculating surface roughness

Surface roughness is calculated by determining the standard deviation of curvature ($C$) for each mapped dune area, defined by a map polygon. This calculation of $\sigma_C$ is utilized because $C$ distributions are centred at 0 (Patton et al., 2018), making it possible to compare dunes without biases introduced by broad-scale topography (e.g. variations in initial morphology caused from the antecedent topography) (Patton et al., 2022). Curvature was generated in ArcMap, which utilizes equations from Moore et al. (1991) and Zevenbergen and Thorne (1987) that calculate curvature from the slope as a percentage and reverse the sign (negative curvature convention). Therefore, we divide ArcMap's curvature output by −100 such that positive values represent concavity (hollows/foot-slopes) and negative values represent convexity (ridges/crest); see the online Supplementary Information and Figure S1. It is important to highlight that $\sigma_C$ values are sensitive to methodology and boundary conditions and/or processes. Minor variabilities in $\sigma_C$ values may occur, but overall trends remain consistent.

Prior to the $\sigma_C$ calculation, we chose to resample the original DEM using bilinear interpolation to 5 m resolution. The reduction in resolution dampened noise and lowered elevation uncertainty by removing DEM processing artefacts and vegetation effects (Berti et al., 2013) while preserving dune morphology (Patton et al., 2022). Our assumption in calibrating a $\sigma_C$–age relationship was that dune $\sigma_C$ values decline monotonically with dune age. Hence, we limited our areas of calibration and application to where diffusive processes and not advective processes (e.g. wind and fluvial transport, which can increase relief and roughness) prevailed. Additionally, all water (water bodies, bogs, coastal cliffs, etc.) and/or anthropogenic modifications (roads, built-up areas, mining, etc.) were also excluded. Once removed, the 'zonal statistics' tool in ArcMap was used to determine $\sigma_C$.

### 3.3 | Optically stimulated luminescence dating

OSL dating provides an age estimate of the time since quartz grains were last exposed to sunlight (burial) (Huntley et al., 1985); therefore, OSL dates represent timing of dune emplacement (Lancaster, 2008). For each dune, OSL samples were collected at dune crests utilizing a sand auger with a 15 cm bucket. Dune stratigraphy was described using standard field protocols (i.e. grain size, sorting, roundness, bedding structures, Munsell colour, and texture). An OSL sampling head was attached with an aluminium insert and once the sample was recovered, the tube was capped, sealed, and stored for later analysis. Dose rate and moisture content samples were collected from the auger samples above and below the OSL sample depth. Eight samples were collected, dating six dunes. On two dunes, we collected multiple OSL samples to increase confidence in measured ages and field interpretations. One dune had samples from the same auger hole and is believed to be equivalent in age. The other dune had samples collected on separate parallel ridges on a transgressive wave, and these ages may vary slightly. These ages are used to supplement those previously collected and reported by Ellerton et al. (2020), Köhler et al. (2021), and Walker et al. (2018).

All OSL samples were processed and analysed at the Utah State University Luminescence Laboratory. Ages were determined utilizing single-aliquot regenerative dose (SAR) analysis of small aliquots of quartz sand (Murray & Wintle, 2000; Murray et al., 2021). Samples were analysed using small aliquot (~10 grains) analysis to reduce scatter caused by grain-to-grain variability in dose rate (micro-dosimetry) (e.g. Ellerton et al., 2020; Guérin et al., 2015). Sample preparation followed standard luminescence protocols (i.e. Wintle, 1997).

All dose rates were determined using representative sub-samples that were analysed using ICP-MS and ICP-AES techniques to determine the concentrations of K, Rb, Th, and U in the sediment. Moisture content (*in situ*) was calculated for all samples. If the measured value was below 5%, we assumed a value of 5 ± 2%, which represents the average moisture history (Ellerton et al., 2020). Dose rates are determined from sediment chemistry, cosmic ray contribution, and water content (Aitken, 1998; Aitken & Xie, 1990) using conversion factors from Guérin et al. (2011). The contribution of cosmic radiation to the dose rate was calculated using sample depth, elevation, and latitude/longitude following the calculations of Prescott and Hutton (1994).

Optical measurements were performed on small aliquot (1 mm diameter, ~10 grains per disk) samples using Risø TL/OSL Model DA-20 readers with blue–green light-emitting diodes (LEDs) (470 ± 30 nm) as stimulation source. The luminescence signal was measured through 7.5 mm ultraviolet filters (U-340) over 40–60 s (250 channels) at 125°C with LED diodes at 70–90% power (~45 mW/cm$^2$) and calculated by subtracting the average of the last 5 s (background signal) from the first 0.7 s (four channels) of the signal decay curve. The luminescence signals show rapid decay dominated by the fast component of the signal (Murray & Wintle, 2003). For those samples with <1 Gy equivalent dose ($D_E$), dose-response curves were fitted linearly between the zero dose and repeated regenerative doses. Results of a preheat-plateau dose-recovery (PP-DR) test (Wintle & Murray, 2006) suggest that a 200°C preheat for 10 s produces the best results for samples in this study. $D_E$ values were calculated using the Central Age Model (CAM) of Galbraith and Roberts (2012) using at least 14 accepted aliquots of quartz sand. Aliquots were rejected if they had evidence of feldspar contamination, a recycling ratio beyond 20% of unity (<0.8 or >1.2), recuperation >1 Gy, or natural $D_E$ greater than the highest regenerative dose given. Errors in $D_E$ and age estimates are reported at 1σ standard error and include errors related to instrument calibration and dose rate/equivalent dose calculations. Errors were calculated in quadrature using the methods of Aitken and Alldred (1972) and Guérin et al. (2011).

### 3.4 | Criteria for utilizing previously OSL-dated dunes

We utilize the following sampling criteria for dune ages from previously published studies. (1) Dates must reflect the age of the dune surface morphology (i.e. the uppermost dune unit that forms the surface morphology was dated). (2) Dunes must be emplaced (i.e. stabilized, not active). Lastly, (3) ages must be collected from dune apices or the crest of the trailing ridges and in physically little altered (B/C, C, soil parent material) soil horizons. These criteria were set to ensure that ages represented primary aeolian deposition.

### 3.5 | Surface roughness–age analysis and age extrapolation

A signal empirical relationship was generated using all OSL-dated dunes within the CSM. We hypothesize that both the CSM and K'gari dune fields are governed by identical mechanisms controlling dune activation and evolution, because they were once part of a connected dune field (Köhler et al., 2021) and have been mapped as part of the same dune system (Patton et al., 2019; Ward, 2006). As a result, we assume that we can apply the same $\sigma_C$–age relationship at both sites.

For use in the $\sigma_C$–age model and validation subset, where dunes have multiple dates, we preferentially selected ages that were collected nearest to the dune crest and/or from sand with minimal pedogenic alterations (C-horizon). Any ages that met our sampling criteria but were not used in the model are recorded. All OSL-dated dunes from the CSM were utilized to build our $\sigma_C$–age model (model set). The remaining OSL-dated dunes from the Inskip Peninsula and K'gari are used as validation subset. We fit our $\sigma_C$–age data with an

exponential curve, given that relief lowers through diffusional processes with time (Booth et al., 2017; LaHusen et al., 2020; Patton et al., 2022). We demonstrate our model output by predicting dune ages from our validation subset, and using reduced major-axis regression we compare the slope of the predicted versus measured dune ages to 1.

A map of estimated dune ages is produced using our $\sigma_C$–age model to convert dune $\sigma_C$ to time since dune emplacement. Mapped dune polygons are reclassified to their estimated ages. Given that the $\sigma_C$–age relationship is constructed from dunes that are emplaced, we do not predict ages for active sections of the dune field, but rather assign them absolute ages of 0 ka. Active sections are identified by aerial imagery as landforms constructed with little to no vegetation and steep lee faces with gradients > 0.65 m m$^{-1}$ (slopes > 33°, which is at or above the angle of repose). All areas previously removed during the calculation of $\sigma_C$ (e.g. sections of dunes with water bodies or anthropogenic disturbances) are incorporated back into the total area to show the full extent of the dune fields and produce the final predictive age map, but their surface roughness is not incorporated in the results.

### 3.6 | Determination of dune emplacement through time

To evaluate the frequency of dune emplacement through time, we determine cumulative probability density functions (PDFs) for the K'gari, CSM, and combined Holocene dune fields (not including active sections). We calculate separate PDFs for OSL-dated and modelled dune ages with 0.05 kyr bin intervals for 12 kyr (240 total bins) and assume that the age estimates represent the median value with normally distributed errors. As a conservative estimate of error, we utilize a constant 10% relative standard error (RSE) for predictive age, which is frequently applied for OSL dating (Murray et al., 2021). We normalize each PDF by total number of dunes used to generate the curve. Additionally, PDFs produced from predictive ages are also normalized by dune area (dune area divided by total Holocene dune area—not including active dune area). This is to remove bias towards younger dunes caused by the preservation of numerous small, younger dunes. We visually compare PDFs and assess dune emplacement through time.

### 3.7 | Sensitivity analysis

We calculate $\sigma_C$ for all map dune polygons at a range of DEM resolutions (1–50 m). For each resolution, a $\sigma_C$–age relationship is produced and its $r^2$ and RMSE are recorded. We predict all dune ages and generate cumulative PDFs utilizing these relationships and their respective DEM resolutions. We compare all PDFs to the OSL-derived PDF. Although the latter does not provide a quantitative assessment of our analysis, it does offer a sense of uncertainty and a foundation to examine how enhanced resolution and bin intervals may influence our interpretations.

## 4 | RESULTS

### 4.1 | OSL results and previously reported OSL ages

The eight newly acquired OSL ages from six individual dunes are shown in Table 1 and Figure 3. For each sample, supporting information such as soil descriptions, geochemistry, water content, and overdispersion are found within the online Supplementary Information (Figure S2; Tables S1 and S2). From previously published work, 20 OSL ages met our sample criteria, dating 16 dunes (specifically Ellerton et al., 2020; Köhler et al., 2021; Walker et al., 2018) (Table 2, Figure 3). All dunes with multiple ages were consistent with our expectations. Samples collected from the same auger hole indicate equivalent ages (e.g. Dune 11), whereas samples from different locations from the same dune yielded ages that increased consistently, moving towards the dune's inland limit (e.g. Dunes 16 and 17). In total (newly acquired and previously published), 28 OSL ages met our criteria, dating 22 dunes. All ages that met our sampling criteria but were not preferred are denoted by italicized text in Table 2.

### 4.2 | Surface roughness–age relationship

The dune calibration ages ($n = 16$) span from 0.23 ± 0.05 ka to 9.82 ± 0.98 ka with surface roughness declining from 0.068 to 0.016 m$^{-1}$ with age (see Table 2). An exponential regression fits our data well, dune age = 32.1 * exp(−108.9 * $\sigma_C$), with $r^2 = 0.942$,

**TABLE 1** OSL results and map location

| Dune number | Map ID | Location | Depth (m) | Lab number | Number of aliquots[a] | Dose rate (Gy/kyr)[b] | Equivalent dose ($D_E$)$^2$ ± 2σ (Gy)[c] | OSL age ± 1σ (ka) |
|---|---|---|---|---|---|---|---|---|
| 4 | 4 | K'gari | 1–1.13 | USU-2742 | 20 (34) | 0.59 ± 0.04 | 0.27 ± 0.07 | 0.45 ± 0.07 |
| 5 | 5 | K'gari | 1–1.16 | USU-2743 | 14 (35) | 0.34 ± 0.03 | 0.16 ± 0.06 | 0.47 ± 0.10 |
| 6 | 6 | K'gari | 1.97–2.24 | USU-2730 | 16 (22) | 0.40 ± 0.03 | 0.51 ± 0.07 | 1.27 ± 0.16 |
| 11 | 11a | CSM | 1.90–2.05 | USU-3020 | 19 (31) | 0.56 ± 0.04 | 1.41 ± 0.23 | 2.51 ± 0.32 |
| 11 | 11a′ | CSM | 3.88–4.07 | USU-3021 | 20 (32) | 0.62 ± 0.04 | 1.33 ± 0.23 | 2.14 ± 0.27 |
| 12 | 12 | K'gari | 4.40–4.50 | USU-2397 | 17 (31) | 0.25 ± 0.03 | 1.00 ± 0.14 | 4.05 ± 0.63 |
| 17 | 17a | K'gari | 3.15–3.20 | USU-2390 | 18 (22) | 0.30 ± 0.03 | 1.79 ± 0.21 | 5.96 ± 0.82 |
| 17 | 17b | K'gari | 3.05–3.15 | USU-2389 | 20 (27) | 0.35 ± 0.03 | 2.5 ± 0.27 | 7.24 ± 0.92 |

[a]OSL age analysis using the single-aliquot regenerative dose procedure of Murray and Wintle (2000) on 1 mm small aliquots of quartz sand. Number of aliquots used in age calculation and number of aliquots analysed in parentheses.
[b]See online Supplementary Information for radioisotope concentrations of surrounding sediment and cosmic contribution to dose rate.
[c]Equivalent dose ($D_E$) calculated using the Central Age Model (Galbraith & Roberts, 2012).

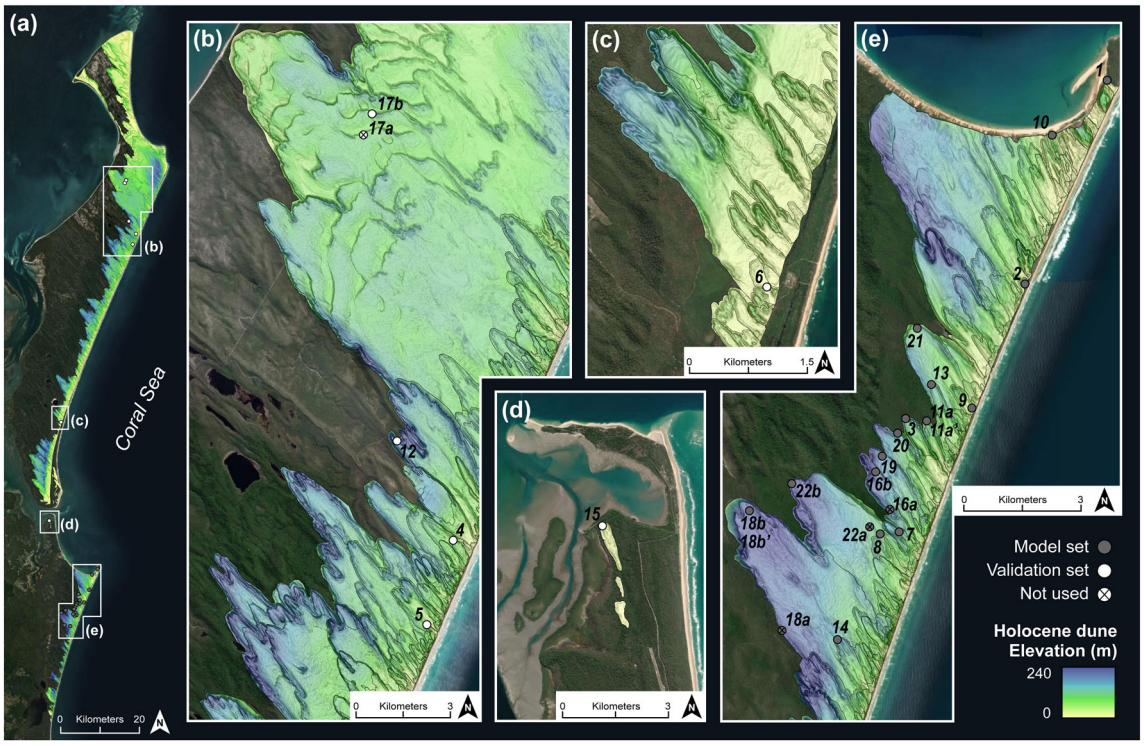


**FIGURE 3** Locations of OSL-dated dunes used in this study. Dunes utilized in our $\sigma_C$–age relationship are represented by grey dots, whereas dunes used in the validation subset are white. For dunes with multiple dates, we preferentially selected ages from crest and/or stratigraphically lower positions. Samples that met our selection criteria but were not used in our model are marked with an 'X'

RMSE = 0.892 ka, and $p$-value < 0.0001 (Figure 4a). Our validation subset from dunes on K'gari and Inskip Peninsula ($n = 6$) falls within the predictions of our model set and demonstrates the predictive power of this model, with a slope of 0.805 (Figure 4b). Similar to past studies, high $\sigma_C$ associated with younger dunes rapidly decreases within the first 1000 years, and after this period $\sigma_C$ values decrease more gradually, which is best described by a negative exponential function (Booth et al., 2017; LaHusen et al., 2020; Patton et al., 2022).

## 4.3 | Predicted dune ages and their spatial relationships and characteristics

In this study, we remotely mapped 92 and 11 active dunes (total 103), and 535 and 191 emplaced Holocene dunes (total 726) on K'gari and the CSM, respectively, covering a total area of 640 km$^2$—33% of both dune fields' total land area. Utilizing the $\sigma_C$–age function above, we estimate the emplacement ages for the Holocene dunes. Generally, the oldest dunes (lowest surface roughness) were located further inland, despite having large sections onlapped by subsequent dune emplacement (Figure S3). Dunes become progressively younger moving towards the east coast (west to east) (Figures 5 and S3). The oldest dunes tend to be larger and less numerous across the landscape, whereas younger dunes are smaller in size but greater in number (Figure S3). Onlapping relationships revealed by the roughness analysis obey the principle of superposition, consistently showing younger dunes superimposed on older dunes.

## 4.4 | Temporal frequency of dune emplacement

Overall, there is good visual correspondence between PDF peaks from the OSL age control and predicted dune ages (Figure 6 vertical teal areas). Utilizing dated dunes and their measurement error ($n = 22$), PDFs depict four major peaks that occur at 0.5, ~2.2, ~4, and ~9.5 ka. When separating the OSL ages into two unique PDFs for both locations, we observe similar trends between K'gari ($n = 6$) and the CSM ($n = 16$), suggesting our sampling efforts captured consistent emplacement events despite having limited OSL dates (white PDFs in Figures S4b and c, respectively).

Using predicted ages derived from the $\sigma_C$–age model (not including active dunes) ($n = 726$), we produce PDFs for dune emplacement. PDFs derived from non-normalized estimated dune ages depict one major significant peak at ~1 ka that rapidly decreases with increasing dune age (Figure 6b). This is observed for both the combined and separated PDFs and is a reflection of the abundant number of mapped dunes (~60%) emplaced during the last 1 kyr (Figure S3a). When accounting for dune area, the combined normalized PDF has four peaks centred at <0.5, ~1.5, ~4, and ~8.5 ka (Figure 6c). The same peaks are common to the PDFs generated for the two areas when treated separately (Figures S4b and c).

## 4.5 | Sensitivity analysis

Surface roughness–age relationships for a range of DEM resolutions (1–50 m) and their associated $r^2$ and RMSE are reported in Table S3.

**TABLE 2** All dunes with their locations (Figure 3) and ages utilized in this study. Note: all italicized rows indicate the OSL ages that are not used in the $\sigma_C$–age model and validation sets and are indicated with an 'X' in Figure 3

| Dune number | Map ID | Location | Latitude, longitude (°S, °E) | Surface roughness ($m^{-1}$) | Model or validation set | Lab number | Mean depth (m) | OSL age ± 1σ (ka) | Study |
|---|---|---|---|---|---|---|---|---|---|
| 1 | 1 | CSM | 25.93, 153.18 | 0.0684 | Model | USU-2011 | 7.40 | 0.23 ± 0.05 | Ellerton et al. (2020) |
| 2 | 2 | CSM | 25.98, 153.16 | 0.0506 | Model | USU-2010 | 1.50 | 0.43 ± 0.06 | Ellerton et al. (2020) |
| 3 | 3 | CSM | 26.01, 153.13 | 0.0368 | Model | USU-2283 | 2.19 | 0.44 ± 0.10 | Ellerton et al. (2020) |
| 4 | 4 | K'gari | −25.16, 153.27 | 0.0465 | Validation | USU-2742 | 1.07 | 0.45 ± 0.12 | This study |
| 5 | 5 | K'gari | 25.19, 153.26 | 0.0593 | Validation | USU-2743 | 1.08 | 0.47 ± 0.18 | This study |
| 6 | 6 | K'gari | 25.60, 153.08 | 0.0406 | Validation | USU-2730 | 2.20 | 1.27 ± 0.22 | This study |
| 7 | 7 | CSM | 26.04, 153.12 | 0.0275 | Model | USU-2267 | 3.45 | 1.94 ± 0.28 | Ellerton et al. (2020) |
| 8 | 8 | CSM | 26.04, 153.12 | 0.0154 | Model | Map 2 Sample 2 | 0.80 | 3.6 ± 0.30 | Walker et al. (2018) |
| 9 | 9 | CSM | 26.01, 153.14 | 0.0236 | Model | USU-2265 | 2.15 | 2.37 ± 0.23 | Ellerton et al. (2020) |
| 10 | 10 | CSM | 25.95, 153.16 | 0.0191 | Model | USU-2012 | 3.25 | 3.53 ± 0.38 | Ellerton et al. (2020) |
| 11 | *11a* | *CSM* | *26.01, 153.13* | – | – | *USU-3020* | *1.98* | *2.51 ± 0.32* | *This study* |
| 11 | 11a′ | CSM | 26.01, 153.13 | 0.0268 | Model | USU-3021 | 4.00 | 2.14 ± 0.27 | This study |
| 12 | 12 | K'gari | 25.13, 153.25 | 0.0189 | Validation | USU-2397 | 4.45 | 4.05 ± 0.80 | This study |
| 13 | 13 | CSM | 25.13, 153.25 | 0.0178 | Model | USU-2284 | 3.62 | 4.89 ± 0.45 | Ellerton et al. (2020) |
| 14 | 14 | CSM | 26.06, 153.11 | 0.0200 | Model | Map 3 Sample 3 | 0.85 | 4.2 ± 0.40 | Walker et al. (2018) |
| 15 | 15 | Inskip | 25.82, 153.05 | 0.0190 | Validation | USU-2744 | 2.55 | 4.84 ± 0.46 | Köhler et al. (2021) |
| 16 | *16a* | *CSM* | *26.02, 153.12* | – | – | *USU-2268* | *8.90* | *5.91 ± 0.61* | *Ellerton et al. (2020)* |
| 16 | 16b | CSM | 26.03, 153.12 | 0.0138 | Model | USU-2269 | 1.48 | 6.96 ± 0.71 | Ellerton et al. (2020) |
| 17 | *17a* | *K'gari* | *25.04, 153.24* | – | – | *USU-2390* | *3.15* | *5.96 ± 1.03* | *This study* |
| 17 | 17b | K'gari | 25.04, 153.25 | 0.0120 | Validation | USU-2389 | 3.10 | 7.24 ± 1.13 | This study |
| 18 | *18a* | *CSM* | *26.06, 153.09* | – | – | *Map 6 Sample 7* | *0.75* | *6.7 ± 0.60* | *Walker et al. (2018)* |
| 18 | *18b* | *CSM* | *26.03, 153.08* | – | – | *Map 4 Sample 4* | *0.80* | *6.2 ± 0.80* | *Walker et al. (2018)* |
| 18 | 18b′ | CSM | 26.03, 153.08 | 0.0113 | Model | Map 4 Sample 5 | 1.05 | 9.8 ± 0.80 | Walker et al. (2018) |
| 19 | 19 | CSM | 26.02, 153.12 | 0.0120 | Model | USU-2282 | 6.85 | 8.17 ± 0.82 | Ellerton et al. (2020) |
| 20 | 20 | CSM | 26.02, 153.12 | 0.0138 | Model | USU-2270 | 1.48 | 9.1 ± 0.96 | Ellerton et al. (2020) |
| 21 | 21 | CSM | 25.99, 153.13 | 0.0108 | Model | USU-2285 | 2.62 | 9.82 ± 0.98 | Ellerton et al. (2020) |
| 22 | *22a* | *CSM* | *26.03, 153.10* | – | – | *Map 5 Sample 6* | *0.80* | *8.3 ± 0.70* | *Walker et al. (2018)* |
| 22 | 22b | CSM | 26.04, 153.12 | 0.0109 | Model | USU-2748 | 6.40 | 9.74 ± 0.90 | Ellerton et al. (2020) |

We find that a wide range of resolutions provide a good fit (3–20 m), with $r^2 > 0.90$ and RMSE < 1.1 ka, with the best resolutions being 5 and 6 m. We observe the poorest relationship (low $r^2$ and high RMSE) for the highest and lowest resolutions (1 and 50 m). Generally, we observe that PDFs determined from DEM resolution between 3 and 20 m show similar frequency, magnitude, and timing of dune emplacement compared to PDFs derived from measured OSL-dated dunes (Table S3, Figure S5).

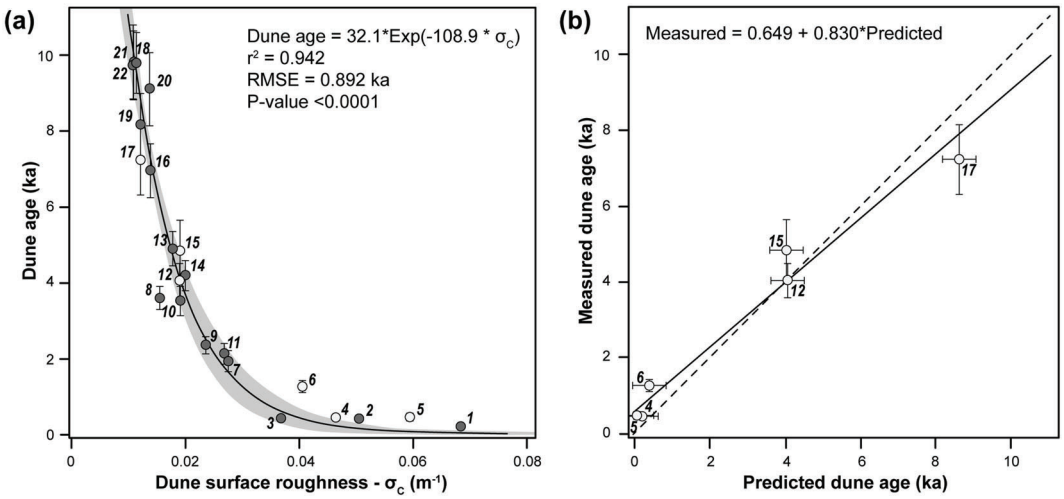


**FIGURE 4** Calculated $\sigma_C$–age relationship from measured OSL-dated dunes. (a) Dune $\sigma_C$ depicts a strong exponential relationship with age ($\pm 1\sigma$) (black line) bounded by 95% confidence intervals (shaded area) within the CSM and K'gari dune fields. Our calibration ages (grey dots) come from the CSM ($n = 18$), whereas the remaining dates used as a validation subset (white dots) come from Inskip and K'gari ($n = 6$). (b) Model validation using predicted versus measured dune ages and their associated best-fit line (black line) using reduced major-axis regression to account for uncertainty in both variables compared to a 1:1 line (solid black dashed line)

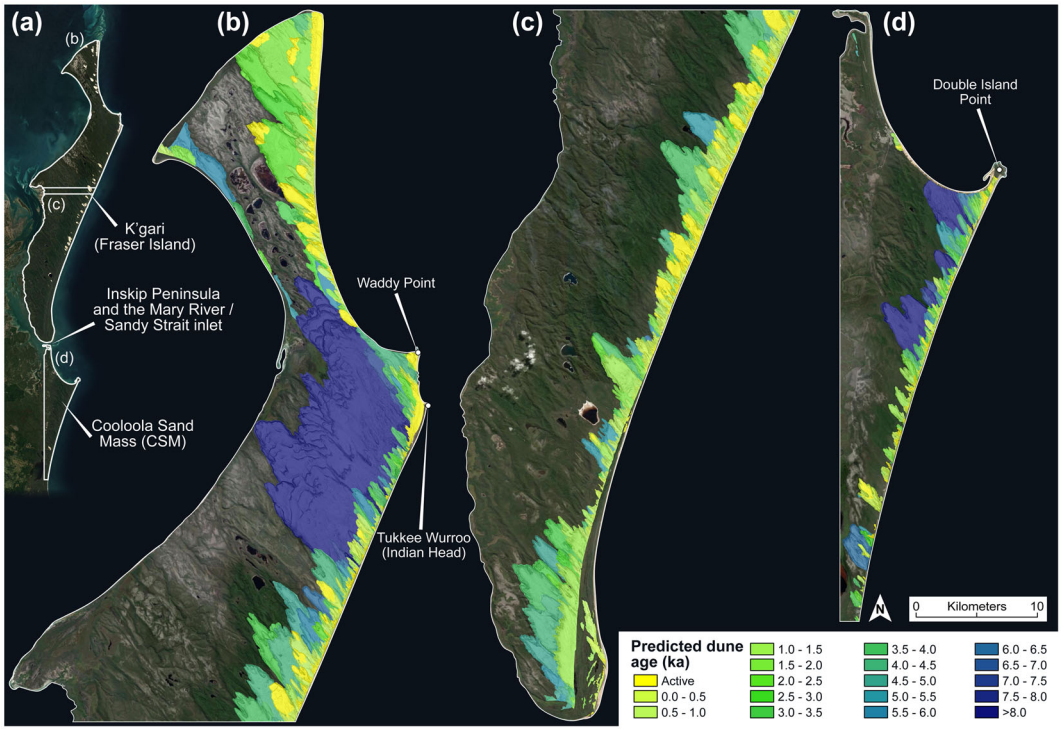


**FIGURE 5** Predicted Holocene dune ages using $\sigma_C$–age model. (a) Aerial imagery of K'gari to the north and the CSM to the south with locations of panels (b) northern K'gari, (c) southern K'gari, and (d) CSM

## 5 | DISCUSSION

### 5.1 | Dune surface roughness and evolutionary processes

While dunes are active, they are dominated by wind advection and deflation that controls their movement near the lee-slope slip face (Hesp, 2002; Pye, 1982). The migrating dunes' surfaces are barren of vegetation, with shallow stoss gradients and over-steepened lee faces that are smooth (low $\sigma_C$). The dune continues to move while vegetation begins to stabilize dune segments along the trailing arms and furthest from the active sections (Levin, 2011; Yan & Baas, 2017). Topographic variability begins to emerge as sand is entrained within and/or forced around vegetation patches. This increases local relief, roughening the dune surface and resulting in an increase in $\sigma_C$. This progresses until the vegetation has fully covered and stabilized the dune's surface, marking the onset of dune emplacement and the highest recorded $\sigma_C$ values (Figure S6). Our observations match those seen in other dune systems

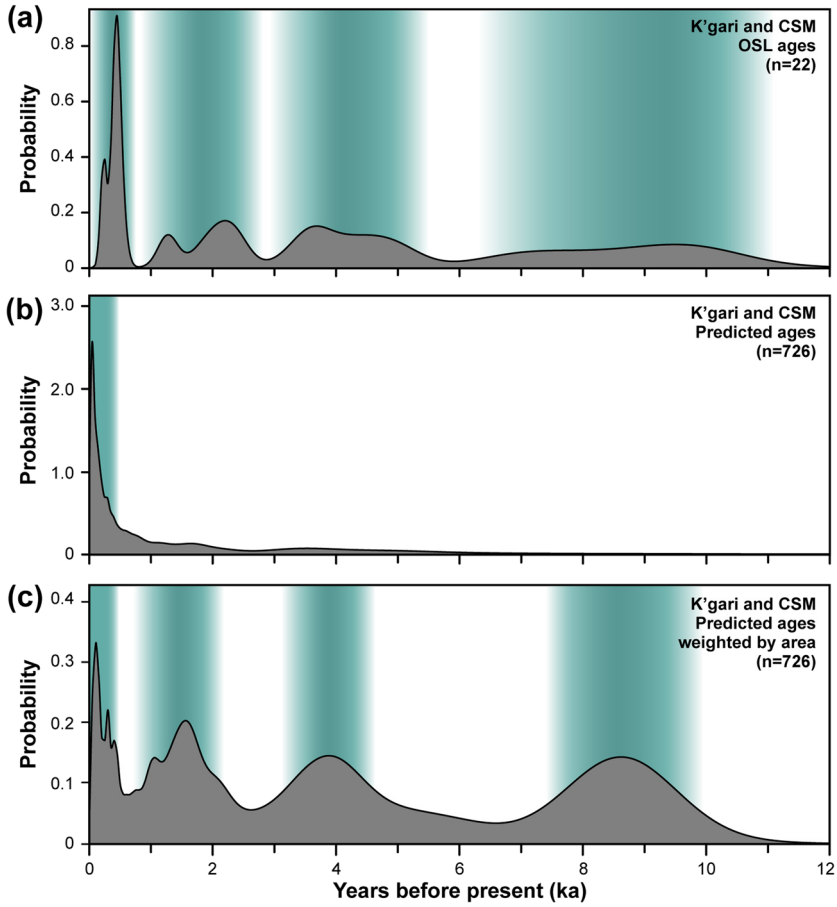


**FIGURE 6** Normalized probability density functions (PDFs) of the combined K'gari and CSM dune fields derived from (a) OSL-dated dunes and (b) predicted ages. (c) Predicted ages normalized by total dune area. Vertical teal areas highlight phases of dune emplacement. By far the largest number of dunes are small coastal blowouts, but cumulatively these dunes represent very little land area and are of only local significance. Area occupied by the dunes is critical as during major activation phases, blowouts coalesce into much larger parabolic and transverse dune fields

(e.g. Hesp, 2002; Pelletier et al., 2009; Stallins & Parker, 2003), indicating that dune emplacement through to the stage of vegetation stabilization is a mechanism that roughens topography.

Once dunes are emplaced, their topographic evolution can be described by diffusive sediment transport theory, which includes two phases of smoothing (decreasing $\sigma_C$ with time) (Patton et al., 2022). The first phase of rapid smoothing is induced by frequent episodic transport from dry ravel and sheetwash processes. This persists until all slopes are lowered below their angle of repose. This is followed by the second phase, which is dominated by slow and continuous transport processes such as bioturbation and granular relaxation. We hypothesize that this will continue as erosion rates lower and the styles of transport become increasingly uniform until no relief remains, $\sigma_C \rightarrow 0\ m^{-1}$ (Figure S6). This general evolution is supported by our field observations that steep slopes persist on young dunes (<1 ka), geomorphic processes are consistent on K'gari, and the validation subset fits well.

## 5.2 | Timing of dune emplacement and regional story

The $\sigma_C$–age relationship calibrated from the CSM accurately predicts the ages of the OSL-dated dunes on K'gari. The findings support the idea that both dune fields are part of the same system, undergoing similar evolutionary development with distinct emplacement phases in the Holocene (e.g. Ellerton et al., 2020; Patton et al., 2019; Ward, 2006). Critically, we are able to predict the age of every emplaced Holocene dune in the dune field, which significantly amplifies our ability to extract chronological signals from dune fields that have, to this point, been limited.

Our approach allows us to observe patterns within the dune fields that would otherwise be obscure. For example, the oldest of the Holocene emplacement phases at the CSM and K'gari is the so-called 'Triangle Cliff' unit (Patton et al., 2019; Ward, 2006). This is comprised of large parabolic dunes, and more locally, large transverse dune waves. This unit was mapped uniformly across the dune fields (Patton et al., 2019; Ward, 2006), suggesting that the entire coastline was simultaneously active during the early Holocene. This is consistent with the expectation that the dune fields would generally be active during the main post-glacial transgression (e.g. Cook, 1986; Lees, 2006; Pye, 1983; Pye & Bowman, 1984; Shulmeister & Lees, 1992; Thom, 1978; Thompson, 1981). However, the age estimates indicate a slightly different pattern; we observe the main preservation of these older Holocene dunes immediately (within ~20 km) south of rocky headlands (i.e. Double Island Point on the CSM; Tukkee Wurroo [aka Indian Head] and Waddy Point on K'gari) (Figure 5). We hypothesize that these headlands act as pinning points for the beaches and long-term rotation of the coastline into swash alignment south of the headlands, which has resulted in enhanced erosion and the consequential loss of older Holocene dunes in the southern parts of both dune fields (Stephens et al., 1981). In addition, eroded sediment tends to accumulate south of the headlands, as can be observed inland from Tukkee Wurroo. The one exception is near the southern limit of K'gari, where the northward migration of the Mary River/Sandy Strait inlet during the Mid- to Late Holocene (Köhler et al., 2021) has increased local sediment supply, promoting

coastal accretion (Figure 5). This has consequently preserved some Mid-Holocene parabolic dunes behind beach–ridge complexes.

Paleoenvironmental interpretations from dune fields are constrained by dune chronologies and are often based on a handful of ages (e.g. Shulmeister & Lees, 1992). In fact, many of the current interpretations for the coastal dune fields are from sparse datasets which are limited to inferred key events, for example, the onset/intensification of the El Niño Southern Oscillation (ENSO) or even the post-glacial transgression. Our method provides a systematic and inexpensive means to substantially expand these chronologies, and a way to increase the robustness of interpretations by providing realistic ages for all the dunes in the dune field. The enhanced chronology is important because patterns of dune activation and emplacement are complex and may encompass significant, region-dependent, time lags and local signals (Lancaster et al., 2016).

## 5.3 | Dune emplacement ages and sea-level variability

Overall, the predicted ages support previous inferences about the dune fields. Whether the SEQ dune fields, including the CSM and K'gari, have been activated by sea-level or climate change has been strongly debated (e.g. Ellerton et al., 2020; Thompson, 1981; Walker et al., 2018; Ward, 1978; Young et al., 1993), but the idea that the main dune-forming events were associated with the glacial maximum has become embedded in the popular literature (e.g. the listing for the Fraser Island/K'gari World Heritage Area). The most comprehensive chronology comes from Ellerton et al. (2020), who constrained the ages of the mapped Pleistocene and Holocene dune units and related these emplacement phases to sea level. In their study, they noted that sea-level rise is likely the main driver inducing dune activity owing to the erosion of sand from the coast and nearshore, and consequent reworking of sediment into the dune fields (Cooper–Thom model) (Cooper, 1958; Thom, 1978).

We re-examine this hypothesis by comparing our PDF results from the $\sigma_C$–age model with local sea-level curves from Larcombe et al. (1995) and Lewis et al. (2008). Similar to Ellerton et al. (2020), our findings support the Cooper–Thom model. We observe four major peaks in the Holocene at ~0.5, ~1.5, ~4, and ~8.5 ka that are primarily tied to sea-level variability (Figure 7).

The clear advantage of our method compared with OSL-generated PDFs is that the peaks are much better defined. This is particularly true for the two older events, which are larger and more pronounced, while this is not the case for the OSL-derived PDF (Figure 6). To maintain consistency with previous papers, we use names of dune units to represent phases of dune emplacement (Ellerton et al., 2020; Patton et al., 2019; Ward, 2006). The oldest emplacement phase (Triangle Cliff) changes from a poorly defined period between ~6.5 and 11 ka (Ellerton et al., 2020), to a tighter-defined event at 8.5 ± 1.0 ka. This coincides well with the termination of the rapid component of post-glacial transgression (e.g. Larcombe et al., 1995). For the two younger events there is a shift in their peaks, in both cases making the peak slightly younger than the OSL-based peaks. For the Freshwater (~4 ± 0.5 ka) and Station Hill (~1.5 ± 0.5 ka) emplacement phases, the revised ages are clearly younger than the sea-level rise they are interpreted to be associated with. This is sensible as the dune ages reflect the timing of sand burial, hence dune emplacement. New dune activation ceases when sea-level rise stops, but the dunes that are active can remain active for decades to centuries after the initiation process has stopped (e.g. Houser et al., 2015; Levin, 2011; Levin et al., 2017).

The most recent dune emplacement event (Cape) occurred within the last 0.5 kyr, which does not correspond with increased sea level. This phase has been ascribed to increased human activity (Aboriginal fires and European clearance and fires) (Cook, 1986), but it has also been proposed that sea-surface temperatures (SST), specifically the intensification of ENSO and the Interdecadal Pacific Oscillation (IPO), may account for this activation (Levin, 2011). While very little is known about the long-term history of the IPO, its direct effect on beach processes in this area has recently been confirmed (Kelly et al., 2019) and it is associated with a change in incident wave direction and effective wave height (McSweeney & Shulmeister, 2018). More positive IPO conditions in the last few centuries may account for this increased coastal dune formation. There is one caveat. Coastal blowouts are formed continuously and are a function of local storms, fires, and other disturbances, as well as regional events (Hesp, 2002; Levin, 2011). The large number of very young dunes may well simply be a reflection of stochastic process, where these dunes have little long-term preservation potential.

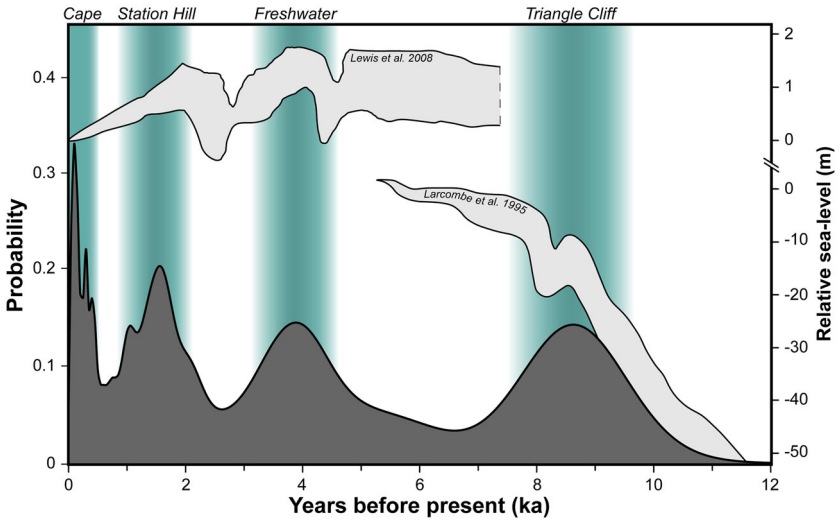


**FIGURE 7** The combined K'gari and CSM dune field PDFs from predicted (dark grey) dune ages compared to local sea-level curves from Larcombe et al. (1995) and Lewis et al. (2008). Note that there is a break in the relative sea-level axis so that both curves could be displayed on the same graph. We observe four emplacement phases (vertical teal areas) that are closely associated with the termination of the rising limb of sea-level events. The addition of our estimated ages permits us to better constrain the timing of dune emplacement (Ellerton et al., 2020), which has been associated with mapped dune units (Patton et al., 2019; Ward, 2006): Cape <0.5 ka; Station Hill ~1.5 ± 0.5 ka; Freshwater ~4 ± 0.5 ka; Triangle Cliff 8.5 ± 1.0 ka

It is important to note that we observe little evidence to support the hypothesis that climate is the major control on widespread dune activity, as proposed by Young et al. (1993) (Figure 8). It has been inferred from paleoclimate records that there was an intensification of ENSO during the mid-Holocene, which may have led to increased storminess and climate variability (Barr et al., 2019; Conroy et al., 2008; Donders et al., 2006; Moy et al., 2002; Shulmeister & Lees, 1995), resulting in widespread dune activity. However, this is unlikely in these dune fields. Pollen studies have shown that vegetation type in the dune field was not modified by climate change in the Holocene. In fact, dune vegetation was remarkably consistent. Instead, any impact of ENSO will be through interactions with the IPO on wave climate and on enhanced SST, triggering more frequent or stronger storms.

## 5.4 | Surface roughness–age model application

In this study we have demonstrated that the $\sigma_C$–age model is a potentially powerful tool to apply in dune settings. The advantage of this approach is that it produces systematic dune ages and only requires high-resolution elevation data and a limited number of constraining dune ages. It also has the ability to detect previously non-identified map units. Dunes can be placed in clusters of similar $\sigma_C$ to help infer the number of emplacement events and their relative sequence, even when dune units are not contiguous and/or age control is absent. Furthermore, reasonable age estimates can be obtained for these undated events. These analyses can be used to target and direct future sampling strategies to ensure all events are confirmed and sampled for dating, while avoiding areas of reactivation so that a robust chronology can be constructed.

In contrast to dune ages, high-resolution elevation data is becoming increasingly available as unmanned aerial vehicles and other remote sensing techniques are being employed extensively to capture topographic information. Indeed, our sensitivity analysis highlights that a wide range of DEM resolutions can produce robust age predictions, the PDFs of which correspond well with previously described emplacement events. We determine that $\sigma_C$ calculated with DEM resolutions of between 3 and 20 m produces similar results. Beyond this range (i.e. finer or coarser resolution), the relationships deteriorate (Table S3, Figure S5). Additionally, it is important to recognize that not all elevation models are equal, and researchers must use their own discretion to determine if their data adequately describe the dune surface at the necessary resolution. For example, for areas with dense vegetation and/or canopy cover, LiDAR should be considered because of its vegetation-penetrating abilities (i.e. bare-earth DEM) rather than a photogrammetry derived DEM which may not capture the 'true topography'.

We expect that our $\sigma_C$–age model will be applicable in many other dune settings. The model has three major assumptions: initial landforms are formed with significant surface roughness, landscape evolution is time dependent, and only diffusive hillslope processes are active. These suggest that all dunes within the same system will have identical evolutionary trajectories ($\sigma_C$–age regression) and their topography will only smooth with time (decreasing $\sigma_C$). Within K'gari and the CSM, these assumptions are known to be valid and are clearly demonstrated by the strength of our model in both locations. Similar to K'gari and the CSM, many coastal dune systems have relatively stable base levels in the Mid- to Late Holocene, well-defined and stable wind fields, and have uniform, well-sorted, and unconsolidated material. These boundary conditions apply on the Oregon coast (Peterson et al., 2007) and Great Lakes of the United States (Hansen et al., 2020), Northern Ireland and Scotland (Sommerville et al., 2007; Wilson et al., 2004), the southeast Brazil coast (Giannini et al., 2007), and Israel (Levin et al., 2008), amongst many others.

Despite superficial similarities, each of these dune systems vary dramatically in climate and biota, which may lead to changes in the rate at which $\sigma_C$ decays with time between sites. As discussed by

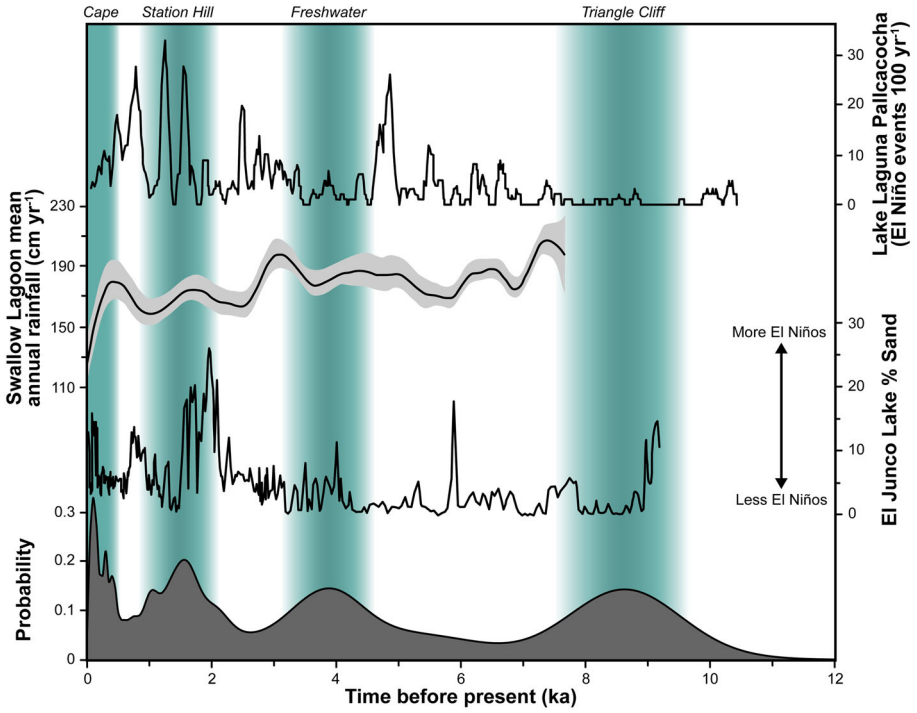


**FIGURE 8** Paleoclimate records through the Holocene from Laguna Pallcacocha in southern Ecuador (Moy et al., 2002), Swallow Lagoon in eastern Australia (Barr et al., 2019), and El Junco Lake in the Galápagos Islands (Conroy et al., 2008) compared to timing of major dune emplacement phases at K'gari and the CSM. Climate appears to have little direct link to dune emplacement

Booth et al. (2017) and Patton et al. (2022), the rate of decline for the regression is controlled by soil diffusivity (which is the combined effect of all environmental factors influencing the efficiency of sediment to move downslope). As a result, there is no one dune field $\sigma_C$–age regression that is applicable at all sites. A new model calibration and validation is critical in each case. Nevertheless, the decline in $\sigma_C$ with time and its value can help infer transport processes, characterize dune evolution, and place tighter constraints on dune-field development with respect to regional climate/sea-level models.

The key limitation of the method is when non-diffusive (advective) processes such as knickpoint erosion also affect dune evolution. For this reason, applications of the method should initially be limited to Holocene dunes and avoid sites with significant fluvial reworking and/or rapid base-level change. Our intention is to adapt the model to Pleistocene sections of the CSM and K'gari dune fields in due course, a process that will involve developing a model that incorporates the effect of base-level changes into the evolving $\sigma_C$.

## CONCLUSIONS

Determining age control for landforms is important within the earth sciences for several reasons, notably providing the rates of processes driving landscape evolution. However, acquiring the volume of ages necessary to develop the complete record of dune emplacement events for a field area is challenging and, in most cases, not feasible. This is mainly due to sample availability, time, cost, and methodological constraints, but may also arise from environmental degradation caused by sampling and travel in sensitive areas. The K'gari and CSM dune fields are ideal locations to validate this approach as within the Holocene, most major factors contributing to landscape evolution can be measured and constrained. We apply an exponential fit to our dune $\sigma_C$–age measurements, and this relationship can be numerically explained through conservation of mass equations. K'gari and the CSM provide a field site where >700 dunes spanning the last 10 kyr are preserved, and which can readily be compared with paleo-records of climate, sea level, and vegetation. Despite numerous dating campaigns, only slightly over 20 luminescence-dated Holocene dunes are reported (Ellerton et al., 2020; Köhler et al., 2021; Tejan-Kella et al., 1990; Walker et al., 2018). This only accounts for <3% of dunes preserved and <1% of the total land area (Patton et al., 2019). To fully understand the spatial and temporal relationship of dune emplacement, many additional ages are required. Utilizing a roughness–age empirical model provides the first high-resolution coastal dune chronology. Its application gives a more robust insight on coastal system evolution than can be derived from limited chronological constraints.

This model provides realistic estimates for every Holocene dune, which is not only useful in understanding where dunes of certain ages are located, but also adds significance to the timing of major dune emplacement events. For example, when only OSL-dated dunes are utilized, the timing of these events is broad and poorly defined. With the addition of the predicted ages, the time constraints on the events narrow, and peaks are more pronounced [e.g. the Triangle Cliff dune unit is reclassified from ~6.5–11 ka by Ellerton et al. (2020) to an 8.5 ± 1.0 ka event]. At K'gari and the CSM, our results confirm that major phases of dune activity are governed by sea-level fluctuations. In addition, the age pattern allows us to demonstrate that their spatial distributions are controlled by changes in swash/drift alignment of the coast. The oldest Holocene dunes are concentrated near headlands that act as pinning points for coastal rotation and are less erosion prone. These observations highlight the power of the method to yield new insights on landform evolution in a coastal dune field.

## ACKNOWLEDGEMENTS

Field work and mapping was undertaken using permit WITK15791415. Funding for this study was provided by the Australian Research Council (ARC) Grant No. DP150101513. We thank the National Parks and Wildlife Service for their assistance. The authors would like to acknowledge the traditional owners of the Cooloola Sand Mass (the Kabi' Kabi' people) and K'gari (the Butchulla people), and thank the Butchulla Aboriginal Corporation (BAC) for their permission and support of work on K'gari (Fraser Island).

## AUTHOR CONTRIBUTIONS

**NRP** conceptualized the idea of the manuscript. **JS** received funding for this project **NRP**, **DE**, **JS**, **TMR**, and **TS** completed all field work. **TMR** and **NRP** carried out dating analyses. **NRP** created applied modelling. **NRP** and **JS** drafted the manuscript. **JS**, **TMR**, and **PCA** are the primary supervisors of NRP. All authors assisted with writing and editing the manuscript.

## DATA AVAILABILITY STATEMENT

All data necessary to generate the results for this study are available in the online Supplementary Information. All LiDAR datasets were downloaded from https://elevation.fsdf.org.au/ and all aerial photographs were downloaded from https://qldglobe.information.qld.gov.au/.

## ORCID

*Nicholas R. Patton* https://orcid.org/0000-0002-4137-0636
*James Shulmeister* https://orcid.org/0000-0001-5863-9462
*Tammy M. Rittenour* https://orcid.org/0000-0003-1925-0395
*Peter Almond* https://orcid.org/0000-0003-4203-1529
*Daniel Ellerton* https://orcid.org/0000-0003-1998-1817
*Talitha Santini* https://orcid.org/0000-0002-6396-3731

## REFERENCES

Aitken, M.J. (1998) *Introduction to Optical Dating: The Dating of Quaternary Sediments by the Use of Photon-Stimulated Luminescence*. Oxford: Clarendon Press.

Aitken, M.J. & Alldred, J.C. (1972) The assessment of error limits in thermoluminescent dating. *Archaeometry*, 14(2), 257–267. Available from: https://doi.org/10.1111/j.1475-4754.1972.tb00068.x

Aitken, M.J. & Xie, J. (1990) Moisture correction for annual gamma dose. *Ancient TL*, 8(2), 6–9.

Atahan, P., Heijnis, H., Dodson, J., Grice, K., Le Metayer, P., Taffs, K., Hembrow, S., Woltering, M. & Zawadzki, A. (2015) Pollen, biomarker and stable isotope evidence of late Quaternary environmental change at Lake McKenzie, southeast Queensland. *Journal of Paleolimnology*, 53(1), 139–156. Available from: https://doi.org/10.1007/s10933-014-9813-3

Barr, C., Tibby, J., Leng, M.J., Tyler, J.J., Henderson, A.C.G., Overpeck, J.T., Simpson, G.L., Cole, J.E., Phipps, S.J., Marshall, J.C., McGregor, G.B., Hua, Q. & McRobie, F.H. (2019) Holocene El Niño–Southern Oscillation variability reflected in subtropical Australian precipitation. *Scientific Reports*, 9(1), 1–9. Available from: https://doi.org/10.1038/s41598-019-38626-3

Bell, R., Petschko, H., Röhrs, M. & Dix, A. (2012) Assessment of landslide age, landslide persistence and human impact using airborne laser scanning digital terrain models. *Geografiska Annaler, Series A: Physical Geography*, 94(1), 135–156. Available from: https://doi.org/10.1111/j.1468-0459.2012.00454.x

Berti, M., Corsini, A. & Daehne, A. (2013) Comparative analysis of surface roughness algorithms for the identification of active landslides. *Geomorphology*, 182, 1–18. Available from: https://doi.org/10.1016/j.geomorph.2012.10.022

Booth, A.M., LaHusen, S.R., Duvall, A.R. & Montgomery, D.R. (2017) Holocene history of deep-seated landsliding in the North Fork Stillaguamish River valley from surface roughness analysis, radiocarbon dating, and numerical landscape evolution modeling. *Journal of Geophysical Research – Earth Surface*, 122(2), 456–472. Available from: https://doi.org/10.1002/2016JF003934

Booth, A.M., Roering, J.J. & Perron, J.T. (2009) Automated landslide mapping using spectral analysis and high-resolution topographic data: Puget Sound lowlands, Washington, and Portland Hills, Oregon. *Geomorphology*, 109(3–4), 132–147. Available from: https://doi.org/10.1016/j.geomorph.2009.02.027

Boyd, R., Ruming, K., Goodwin, I., Sandstrom, M. & Schröder-Adams, C. (2008) Highstand transport of coastal sand to the deep ocean: A case study from Fraser Island, southeast Australia. *Geology*, 36(1), 15–18. Available from: https://doi.org/10.1130/G24211A.1

Coaldrake, J.E. (1962) The coastal sand dunes of southern Queensland. *Proceedings of the Royal Society of Queensland*, 72, 101–116.

Conroy, J.L., Overpeck, J.T., Cole, J.E., Shanahan, T.M. & Steinitz-Kannan, M. (2008) Holocene changes in eastern tropical Pacific climate inferred from a Galápagos lake sediment record. *Quaternary Science Reviews*, 27(11–12), 1166–1180. Available from: https://doi.org/10.1016/j.quascirev.2008.02.015

Cook, P.G. (1986) A review of coastal dune building in Eastern Australia. *Australian Geographer*, 17(2), 133–143. Available from: https://doi.org/10.1080/00049188608702912

Cooper, W.S. (1958) *Coastal sand dunes of Oregon and Washington*. Geological Society of America: Boulder, CO. https://doi.org/10.1130/MEM72-p1

Donders, T.H., Wagner, F. & Visscher, H. (2006) Late Pleistocene and Holocene subtropical vegetation dynamics recorded in perched lake deposits on Fraser Island, Queensland, Australia. *Palaeogeography, Palaeoclimatology, Palaeoecology*, 241(3–4), 417–439. Available from: https://doi.org/10.1016/j.palaeo.2006.04.008

Ellerton, D., Rittenour, T., Miot da Silva, G., Gontz, A., Shulmeister, J., Hesp, P., Santini, T. & Welsh, K.J. (2018) Late-Holocene cliff-top blowout activation and evolution in the Cooloola Sand Mass, southeast Queensland, Australia. *The Holocene*, 28(11), 1697–1711. https://doi.org/10.1177/0959683618788679

Ellerton, D., Rittenour, T., Shulmeister, J., Gontz, A., Welsh, K.J. & Patton, N.R. (2020) An 800 kyr record of dune emplacement in relationship to high sea level forcing, Cooloola Sand Mass, Queensland, Australia. *Geomorphology*, 354, 106999. Available from: https://doi.org/10.1016/j.geomorph.2019.106999

Frankel, K.L. & Dolan, J.F. (2007) Characterizing arid region alluvial fan surface roughness with airborne laser swath mapping digital topographic data. *Journal of Geophysical Research – Earth Surface*, 112, F02025. https://doi.org/10.1029/2006JF000644

Galbraith, R.F. & Roberts, R.G. (2012) Statistical aspects of equivalent dose and error calculation and display in OSL dating: An overview and some recommendations. *Quaternary Geochronology*, 11, 1–27. Available from: https://doi.org/10.1016/j.quageo.2012.04.020

Giannini, P.C., Sawakuchi, A.O., Martinho, C.T. & Tatumi, S.H. (2007) Eolian depositional episodes controlled by Late Quaternary relative sea level changes on the Imbituba–Laguna coast (southern Brazil). *Marine Geology*, 237(3–4), 143–168. Available from: https://doi.org/10.1016/j.margeo.2006.10.027

Gillette, D.A. & Stockton, P.H. (1989) The effect of nonerodible particles on wind erosion of erodible surfaces. *Journal of Geophysical Research – Atmospheres*, 94(D10), 12885–12893. Available from: https://doi.org/10.1029/JD094iD10p12885

Glenn, N.F., Streutker, D.R., Chadwick, D.J., Thackray, G.D. & Dorsch, S.J. (2006) Analysis of LiDAR-derived topographic information for characterizing and differentiating landslide morphology and activity. *Geomorphology*, 73(1–2), 131–148. Available from: https://doi.org/10.1016/j.geomorph.2005.07.006

Goetz, J.N., Bell, R. & Brenning, A. (2014) Could surface roughness be a poor proxy for landslide age? Results from the Swabian Alb, Germany. *Earth Surface Processes and Landforms*, 39(12), 1697–1704. Available from: https://doi.org/10.1002/esp.3630

Guérin, G., Jain, M., Thomsen, K.J., Murray, A.S. & Mercier, N. (2015) Modelling dose rate to single grains of quartz in well-sorted sand samples: The dispersion arising from the presence of potassium feldspars and implications for single grain OSL dating. *Quaternary Geochronology*, 27, 52–65. Available from: https://doi.org/10.1016/j.quageo.2014.12.006

Guérin, G., Mercier, N. & Adamiec, G. (2011) Dose-rate conversion factors: Update. *Ancient TL*, 29(1), 5–8.

Han, M., Kim, J.C., Yang, D.Y., Lim, J. & Yi, S. (2021) The main periods and environmental controls of coastal dune development along the west coast of the Korean Peninsula during the mid to late Holocene. *Palaeogeography, Palaeoclimatology, Palaeoecology*, 569, 110345. Available from: https://doi.org/10.1016/j.palaeo.2021.110345

Hansen, E., DeVries-Zimmerman, S., Davidson-Arnott, R., Dijk, D.V., Bodenbender, B., Kilibarda, Z., Thompson, T. & Yurk, B. (2020) Dunes of the Laurentian Great Lakes. In: Lancaster, N. & Hesp, P. (Eds.). *Inland Dunes of North America*. Cham: Springer, pp. 65–120. https://doi.org/10.1007/978-3-030-40498-7_3

Harrold, AG, McDonald, WJF, Hopkins, MS, Walker, J, Sandercoe, CS, Thompson, CH. 1987. *Studies in landscape dynamics in the Cooloola–Noosa River area, Queensland*. CSIRO: Canberra.

Hesp, P. (2002) Foredunes and blowouts: Initiation, geomorphology and dynamics. *Geomorphology*, 48(1–3), 245–268. Available from: https://doi.org/10.1016/S0169-555X(02)00184-8

Houser, C., Wernette, P., Rentschlar, E., Jones, H., Hammond, B. & Trimble, S. (2015) Post-storm beach and dune recovery: Implications for barrier island resilience. *Geomorphology*, 234, 54–63. Available from: https://doi.org/10.1016/j.geomorph.2014.12.044

Huntley, D.J., Godfrey-Smith, D.I. & Thewalt, M.L. (1985) Optical dating of sediments. *Nature*, 313(5998), 105–107. Available from: https://doi.org/10.1038/313105a0

Jerolmack, D.J., Ewing, R.C., Falcini, F., Martin, R.L., Masteller, C., Phillips, C., Reitz, M.D. & Buynevich, I. (2012) Internal boundary layer model for the evolution of desert dune fields. *Nature Geoscience*, 5(3), 206–209. Available from: https://doi.org/10.1038/ngeo1381

Kelly, J.T., McSweeney, S., Shulmeister, J. & Gontz, A.M. (2019) Bimodal climate control of shoreline change influenced by Interdecadal Pacific Oscillation variability along the Cooloola Sand Mass, Queensland, Australia. *Marine Geology*, 415, 105971. Available from: https://doi.org/10.1016/j.margeo.2019.105971

Köhler, M., Shulmeister, J., Patton, N.R., Rittenour, T.M., McSweeney, S., Ellerton, D.T., Stout, J.C. & Hüneke, H. (2021) Holocene evolution of a barrier–spit complex and the interaction of tidal and wave processes, Inskip Peninsula, SE Queensland, Australia. *The Holocene*, 31(9), 1476–1488. Available from: https://doi.org/10.1177/09596836211019092

Korzeniowska, K., Pfeifer, N. & Landtwing, S. (2018) Mapping gullies, dunes, lava fields, and landslides via surface roughness. *Geomorphology*, 301, 53–67. Available from: https://doi.org/10.1016/j.geomorph.2017.10.011

LaHusen, S.R., Duvall, A.R., Booth, A.M., Grant, A., Mishkin, B.A., Montgomery, D.R., Struble, W., Roering, J.J. & Wartman, J. (2020) Rainfall triggers more deep-seated landslides than Cascadia earthquakes in the Oregon Coast Range, USA. *Science Advances*, 6(38), eaba6790. Available from: https://doi.org/10.1126/sciadv.aba6790

Lancaster, N. (2008) Desert dune dynamics and development: Insights from luminescence dating. *Boreas*, 37(4), 559–573. Available from: https://doi.org/10.1111/j.1502-3885.2008.00055.x

Lancaster, N. & Baas, A. (1998) Influence of vegetation cover on sand transport by wind: Field studies at Owens Lake, California. *Earth Surface Processes and Landforms*, 23(1), 69–82. Available from: https://

doi.org/10.1002/(SICI)1096-9837(199801)23:1<69::AID-ESP823>3.0.CO;2-G

Lancaster, N., Wolfe, S., Thomas, D., Bristow, C., Bubenzer, O., Burrough, S., Duller, G., Halfen, A., Hesse, P., Roskin, J., Singhvi, A., Tsoar, H., Tripaldi, A., Yang, X. & Zárate, M. (2016) The INQUA Dunes Atlas chronologic database. *Quaternary International*, 410, 3–10. Available from: https://doi.org/10.1016/j.quaint.2015.10.044

Larcombe, P., Carter, R.M., Dye, J., Gagan, M.K. & Johnson, D.P. (1995) New evidence for episodic post-glacial sea-level rise, central Great Barrier Reef, Australia. *Marine Geology*, 127(1–4), 1–44. Available from: https://doi.org/10.1016/0025-3227(95)00059-8

Lees, B. (2006) Timing and formation of coastal dunes in northern and eastern Australia. *Journal of Coastal Research*, 22(1), 78–89. Available from: https://doi.org/10.2112/05A-0007.1

Levin, N. (2011) Climate-driven changes in tropical cyclone intensity shape dune activity on Earth's largest sand island. *Geomorphology*, 125(1), 239–252. Available from: https://doi.org/10.1016/j.geomorph.2010.09.021

Levin, N., Ben-Dor, E., Kidron, G.J. & Yaakov, Y. (2008) Estimation of surface roughness ($z_0$) over a stabilizing coastal dune field based on vegetation and topography. *Earth Surface Processes and Landforms*, 33(10), 1520–1541. Available from: https://doi.org/10.1002/esp.1621

Levin, N., Jablon, P.E., Phinn, S. & Collins, K. (2017) Coastal dune activity and foredune formation on Moreton Island, Australia, 1944–2015. *Aeolian Research*, 25, 107–121. Available from: https://doi.org/10.1016/j.aeolia.2017.03.005

Lewis, S.E., Wüst, R.A., Webster, J.M. & Shields, G.A. (2008) Mid–late Holocene sea-level variability in eastern Australia. *Terra Nova*, 20(1), 74–81. Available from: https://doi.org/10.1111/j.1365-3121.2007.00789.x

Lindhorst, S. & Betzler, C. (2016) The climate-archive dune: Sedimentary record of annual wind intensity. *Geology*, 44(9), 711–714. Available from: https://doi.org/10.1130/G38093.1

Marín, L., Forman, S.L., Valdez, A. & Bunch, F. (2005) Twentieth century dune migration at the Great Sand Dunes National Park and Preserve, Colorado, relation to drought variability. *Geomorphology*, 70(1–2), 163–183. Available from: https://doi.org/10.1016/j.geomorph.2005.04.014

Martínez, M.L. & Psuty, N.P. (2004) *Coastal Dunes*. Berlin: Springer Verlag 10.1007/978-3-540-74002-5.

McKean, J. & Roering, J. (2004) Objective landslide detection and surface morphology mapping using high-resolution airborne laser altimetry. *Geomorphology*, 57(3–4), 331–351. Available from: https://doi.org/10.1016/S0169-555X(03)00164-8

McSweeney, S. & Shulmeister, J. (2018) Variations in wave climate as a driver of decadal scale shoreline change at the Inskip Peninsula, southeast Queensland, Australia. *Estuarine, Coastal and Shelf Science*, 209, 56–69. Available from: https://doi.org/10.1016/j.ecss.2018.04.034

Moore, I.D., Grayson, R.B. & Landson, A.R. (1991) Digital terrain modeling: A review of hydrological, geomorphological, and biological applications. *Hydrological Processes*, 5(1), 3–30. Available from: https://doi.org/10.1002/hyp.3360050103

Moss, P., Dudgeon, A., Shapland, F., Withers, L., Brownhall, C., Terzano, D., Petherick, L., & Sloss, C. (2013). Investigation into the Vegetation and Fire History of the EPBC, Ramsar and WHA Wetlands of the Great Sandy Straits, South East Queensland. Unpublished report to the Burnett Mary Regional Group, Bundaberg, Queensland.

Moy, C.M., Seltzer, G.O., Rodbell, D.T. & Anderson, D.M. (2002) Variability of El Niño/Southern Oscillation activity at millennial timescales during the Holocene epoch. *Nature*, 420(6912), 162–165. Available from: https://doi.org/10.1038/nature01194

Murray, A., Arnold, L.J., Buylaert, J.P., Guérin, G., Qin, J., Singhvi, A.K., Smedley, R. & Thomsen, K.J. (2021) Optically stimulated luminescence dating using quartz. *Nature Reviews Methods Primers*, 1(1), 1–31. Available from: https://doi.org/10.1038/s43586-021-00068-5

Murray, A.S. & Wintle, A.G. (2000) Luminescence dating of quartz using an improved single-aliquot regenerative-dose protocol. *Radiation Measurements*, 32(1), 57–73. Available from: https://doi.org/10.1016/S1350-4487(99)00253-X

Murray, A.S. & Wintle, A.G. (2003) The single aliquot regenerative dose protocol: Potential for improvements in reliability. *Radiation Measurements*, 37(4–5), 377–381. Available from: https://doi.org/10.1016/S1350-4487(03)00053-2

Patterson, C.C. & Patterson, D.C. (1983) Gold Coast longshore transport. In: *Proceedings of the 6th Australian Coastal and Ocean Engineering Conference*. Gold Coast: The Institute of Engineers, pp. 251–256.

Patton, N.R., Ellerton, D. & Shulmeister, J. (2019) High-resolution remapping of the coastal dune fields of south east Queensland, Australia: A morphometric approach. *Journal of Maps*, 15(2), 578–589. Available from: https://doi.org/10.1080/17445647.2019.1642246

Patton, N.R., Lohse, K.A., Godsey, S.E., Crosby, B.T. & Seyfried, M.S. (2018) Predicting soil thickness on soil mantled hillslopes. *Nature Communications*, 9(1), 1–10. Available from: https://doi.org/10.1038/s41467-018-05743-y

Patton, N.R., Shulmeister, J., Ellerton, D. & Seropian, G. (2022) Measuring landscape evolution from inception to maturity: Insights from a coastal dune system. *Earth and Planetary Science Letters*, 584, 117448. Available from: https://doi.org/10.1016/j.epsl.2022.117448

Pelletier, J.D. (2013) Deviations from self-similarity in barchan form and flux: The case of the Salton Sea dunes, California. *Journal of Geophysical Research – Earth Surface*, 118(4), 2406–2420.

Pelletier, J.D., Mitasova, H., Harmon, R.S. & Overton, M. (2009) The effects of interdune vegetation changes on eolian dune field evolution: A numerical-modeling case study at Jockey's Ridge, North Carolina, USA. *Earth Surface Processes and Landforms*, 34(9), 1245–1254. Available from: https://doi.org/10.1002/esp.1809

Peterson, C.D., Stock, E., Price, D.M., Hart, R., Reckendorf, F., Erlandson, J.M. & Hostetler, S.W. (2007) Ages, distributions, and origins of upland coastal dune sheets in Oregon, USA. *Geomorphology*, 91(102), 80–102. Available from: https://doi.org/10.1016/j.geomorph.2007.02.005

Pommerol, A., Chakraborty, S. & Thomas, N. (2012) Comparative study of the surface roughness of the Moon, Mars and Mercury. *Planetary and Space Science*, 73(1), 287–293. Available from: https://doi.org/10.1016/j.pss.2012.08.020

Prescott, J.R. & Hutton, J.T. (1994) Cosmic ray contributions to dose rates for luminescence and ESR dating: Large depths and long-term time variations. *Radiation Measurements*, 23(2–3), 497–500. Available from: https://doi.org/10.1016/1350-4487(94)90086-8

Pye, K. (1982) Morphological development of coastal dunes in a humid tropical environment, Cape Bedford and Cape Flattery, North Queensland. *Geografiska Annaler, Series A: Physical Geography*, 64(3–4), 213–227. Available from: https://doi.org/10.1080/04353676.1982.11880067

Pye, K. (1983) Coastal dunes. *Progress in Physical Geography*, 7(4), 531–557. Available from: https://doi.org/10.1177/030913338300700403

Pye, K. & Bowman, GM. (1984) The Holocene marine transgression as a forcing function in episodic dune activity on the eastern Australian coast. In Thom, BG (ed.), *Coastal Geomorphology in Australia*. Academic Press: New York; 179–196.

Raupach, M.R., Gillette, D.A. & Leys, J.F. (1993) The effect of roughness elements on wind erosion threshold. *Journal of Geophysical Research – Atmospheres*, 98(D2), 3023–3029. Available from: https://doi.org/10.1029/92JD01922

Roy, P.S. & Thom, B.G. (1981) Late Quaternary marine deposition in New South Wales and southern Queensland—an evolutionary model. *Journal of the Geological Society of Australia*, 28(3–4), 471–489. Available from: https://doi.org/10.1080/00167618108729182

Schanz, S.A. & Colee, A.P. (In review, 2021) Development of a surface roughness curve to estimate timing of earthflows and habitat development in the Teanaway River, central Washington State, USA. *Earth Surface Dynamics Discussions*. [Preprint]. Available from: https://doi.org/10.5194/esurf-2021-61

Shulmeister, J. & Lees, B.G. (1992) Morphology and chronostratigraphy of a coastal dune field; Groote Eylandt, northern Australia. *Geomorphology*, 5(6), 521–534. Available from: https://doi.org/10.1016/0169-555X(92)90023-H

Shulmeister, J. & Lees, B.G. (1995) Pollen evidence from tropical Australia for the onset of an ENSO-dominated climate at c. 4000 BP. *The Holocene*, 5(1), 10–18. Available from: https://doi.org/10.1177/095968369500500102

Shumack, S. & Hesse, P. (2018) Assessing the geomorphic disturbance from fires on coastal dunes near Esperance, Western Australia: Implications for dune de-stabilisation. *Aeolian Research*, 31, 29–49. Available from: https://doi.org/10.1016/j.aeolia.2017.08.005

Smith, M.W. (2014) Roughness in the earth sciences. *Earth-Science Reviews*, 136, 202–225. Available from: https://doi.org/10.1016/j.earscirev.2014.05.016

Sommerville, A.A., Hansom, J.D., Housley, R.A. & Sanderson, D.C.W. (2007) Optically stimulated luminescence (OSL) dating of coastal aeolian sand accumulation in Sanday, Orkney Islands, Scotland. *The Holocene*, 17(5), 627–637. Available from: https://doi.org/10.1177/0959683607078987

Stallins, J.A. & Parker, A.J. (2003) The influence of complex systems interactions on barrier island dune vegetation pattern and process. *Annals of the Association of American Geographers*, 93(1), 13–29. Available from: https://doi.org/10.1111/1467-8306.93102

Stephens, A., Roy, P. & Jones, M. (1981) Geological model of erosion on a littoral drift coast. In *Proceedings of the 5th Australian Conference on Coastal and Ocean Engineering: Offshore Structures*. Institute of Engineers: Barton, ACT; 174–179. https://search.informit.org/doi/10.3316/informit.925679732664746

Swezey, C. (2001) Eolian sediment responses to late Quaternary climate changes: Temporal and spatial patterns in the Sahara. *Palaeogeography, Palaeoclimatology, Palaeoecology*, 167(1–2), 119–155. Available from: https://doi.org/10.1016/S0031-0182(00)00235-2

Tejan-Kella, M.S., Chittleborough, D.J., Fitzpatrick, R.W., Thompson, C.H., Prescott, J.R. & Hutton, J.T. (1990) Thermoluminescence dating of coastal sand dunes at Cooloola and North Stradbroke Island, Australia. *Soil Research*, 28(4), 465–481. Available from: https://doi.org/10.1071/SR9900465

Thom, B.G. (1978) Coastal sand deposition in southeast Australia during the Holocene. In: Davies, J.L. & Williams, M.A.J. (Eds.). *Landform Evolution in Australasia*. Canberra: ANU Press, pp. 197–214.

Thompson, C.H. (1981) Podzol chronosequences on coastal dunes of eastern Australia. *Nature*, 291(5810), 59–61. Available from: https://doi.org/10.1038/291059a0

Thompson, C.H. (1992) Genesis of podzols on coastal dunes in southern Queensland. I. Field relationships and profile morphology. *Soil Research*, 30(5), 593–613. Available from: https://doi.org/10.1071/SR9920593

Tsoar, H. (2005) Sand dunes mobility and stability in relation to climate. *Physica A: Statistical Mechanics and its Applications*, 357(1), 50–56. Available from: https://doi.org/10.1016/j.physa.2005.05.067

Vimpere, L., Watkins, S.E. & Castelltort, S. (2021) Continental interior parabolic dunes as a potential proxy for past climates. *Global and Planetary Change*, 206, 103622. Available from: https://doi.org/10.1016/j.gloplacha.2021.103622

Walker, J., Lees, B., Olley, J. & Thompson, C. (2018) Dating the Cooloola coastal dunes of south-eastern Queensland, Australia. *Marine Geology*, 398, 73–85. Available from: https://doi.org/10.1016/j.margeo.2017.12.010

Ward, R. (1978) Australian legend re-visited. *Australian Historical Studies*, 18(71), 171–190. Available from: https://doi.org/10.1080/10314617808595586

Ward, W.T. (2006) Coastal dunes and strandplains in southeast Queensland: Sequence and chronology. *Australian Journal of Earth Sciences*, 53(2), 363–373. Available from: https://doi.org/10.1080/08120090500507354

Wells, A. & Goff, J. (2007) Coastal dunes in Westland, New Zealand, provide a record of paleoseismic activity on the Alpine fault. *Geology*, 35(8), 731–734. Available from: https://doi.org/10.1130/G23554A.1

Wiggs, G.F., Livingstone, I., Thomas, D.S. & Bullard, J.E. (1996) Airflow and roughness characteristics over partially vegetated linear dunes in the southwest Kalahari Desert. *Earth Surface Processes and Landforms*, 21(1), 19–34. Available from: https://doi.org/10.1002/(SICI)1096-9837(199601)21:1<19::AID-ESP508>3.0.CO;2-P

Wilson, P. (2002) Holocene coastal dune development on the South Erradale peninsula, Wester Ross, Scotland. *Scottish Journal of Geology*, 38(1), 5–13. Available from: https://doi.org/10.1144/sjg38010005

Wilson, P., McGourty, J. & Bateman, M.D. (2004) Mid- to late-Holocene coastal dune event stratigraphy for the north coast of Northern Ireland. *The Holocene*, 14(3), 406–416. Available from: https://doi.org/10.1191/0959683604hl716rp

Wintle, A.G. (1997) Luminescence dating: Laboratory procedures and protocols. *Radiation Measurements*, 27(5–6), 769–817. Available from: https://doi.org/10.1016/S1350-4487(97)00220-5

Wintle, A.G. & Murray, A.S. (2006) A review of quartz optically stimulated luminescence characteristics and their relevance in single-aliquot regeneration dating protocols. *Radiation Measurements*, 41(4), 369–391. Available from: https://doi.org/10.1016/j.radmeas.2005.11.001

Yan, N. & Baas, A.C. (2015) Parabolic dunes and their transformations under environmental and climatic changes: Towards a conceptual framework for understanding and prediction. *Global and Planetary Change*, 124, 123–148. Available from: https://doi.org/10.1016/j.gloplacha.2014.11.010

Yan, N. & Baas, A.C. (2017) Environmental controls, morphodynamic processes, and ecogeomorphic interactions of barchan to parabolic dune transformations. *Geomorphology*, 278, 209–237. Available from: https://doi.org/10.1016/j.geomorph.2016.10.033

Yizhaq, H., Ashkenazy, Y. & Tsoar, H. (2007) Why do active and stabilized dunes coexist under the same climatic conditions? *Physical Review Letters*, 98(18), 188001. Available from: https://doi.org/10.1103/PhysRevLett.98.188001

Young, R.W., Bryant, E.A., Price, D.M., Wirth, L.M. & Pease, M. (1993) Theoretical constraints and chronological evidence of Holocene coastal development in central and southern New South Wales, Australia. *Geomorphology*, 7(4), 317–329. Available from: https://doi.org/10.1016/0169-555X(93)90061-6

Zevenbergen, L.W. & Thorne, C.R. (1987) Quantitative analysis of land surface topography. *Earth Surface Process Landforms*, 12(1), 47–56. Available from: https://doi.org/10.1002/esp.3290120107

## SUPPORTING INFORMATION

Additional supporting information may be found in the online version of the article at the publisher's website.

**How to cite this article:** Patton, N.R., Shulmeister, J., Rittenour, T.M., Almond, P., Ellerton, D. & Santini, T. (2022) Using calibrated surface roughness dating to estimate coastal dune ages at K'gari (Fraser Island) and the Cooloola Sand Mass, Australia. *Earth Surface Processes and Landforms*, 1–16. Available from: https://doi.org/10.1002/esp.5387